



Improved mechanical properties and corrosion resistance of Zr-Cu-Al-Ni-Ti bulk metallic glass by Fe substitution for Ni



Hongqi Shi^{a,b,d,1}, Hao Zhou^{a,1}, Zhenghao Zhou^a, Yi Ding^{a,c,d,*}, Wenjuan Liu^{a,c,*}, Jin Ji^b

^a College of Materials Science and Engineering, Nanjing Tech University, Nanjing 211816, China

^b School of Information Engineering, Suzhou University, Suzhou 223800, China

^c Jiangsu Collaborative Innovation Center for Advanced Inorganic Functional Composites, Nanjing Tech University, Nanjing 211816, China

^d Suzhou Advanced Materials Industry Technology Innovation Center of Nanjing Tech University, Suzhou 223800, China

ARTICLE INFO

ABSTRACT

Keywords:

Bulk metallic glass
Zr alloy
Mechanical property
Corrosion resistance
Fe substitution

Herein, the effects of Fe substitution for Ni on glass-forming ability (GFA), mechanical properties and corrosion resistance of $Zr_{56}Cu_{24}Al_9Ni_{7-x}Ti_4Fe_x$ ($x = 0, 1, 3, 5$, and 7 at.%) bulk metallic glass (BMGs) were investigated. Trace addition of Fe to 3 at.% slightly affects the GFA of alloys, but Fe over-dosage results in an intense susceptibility to crystallization and failure to form metallic glasses. Furthermore, the compressive strength and plasticity of $Zr_{56}Cu_{24}Al_9Ni_4Ti_4Fe_3$ alloy are significantly enhanced to 1709 MPa and 5.55%, respectively, compared to 1677 MPa and 1.22% for pristine alloy. Meanwhile, the corrosion resistance is greatly improved by Fe addition to 3 at.% then deteriorated with its excess addition. The $Zr_{56}Cu_{24}Al_9Ni_4Ti_4Fe_3$ alloy exhibits the widest passivation zone and the largest R_{ct} , indicating an enhanced corrosion performance. Overall, the synergistic effect of Fe substitution on mechanical and corrosion performance opens a new horizon for design of toxic-free Zr-based BMGs for potential application.

1. Introduction

As emerging amorphous materials, bulk metallic glasses (BMGs), have aroused great scientific concerns due to their unique characteristics and been widely applied in catalytic, wear resistant and biomedical applications since they were developed in 1960s. Among them, Zr-based metallic glasses receive extensive attentions especially in the field of engineering and bio-implant due to their excellent glass-forming ability (GFA), good mechanical properties, biocompatibility, and corrosion resistance [1–4]. Up to now, most of Zr-based BMGs contain Ni element to improve GFA and to possess a superior thermal stability [5,6], however the potential toxicity of Ni inevitably causes allergies or inflammation to patients and considerably limits their biomedical application prospects [7–8]. Accordingly, Ni-free Zr-based BMG systems are emerging to eliminate the allergic and adverse effects for practical biomedical applications. Although there is already a lot Ni-free Zr-based BMGs existed [9–11], the inferior mechanical properties prevent them from the practical bio-implant application. For instance, Li et al. found Ni-free $Zr_{60}Cu_{25}Al_{10}Fe_{5-x}Ag_x$ metallic glass has a plastic deformation rate of 3.7% and an elastic deformation rate of 2.6%, which is too low to

be a biological implant material [10]. Furthermore, BMGs lack macroscopic room-temperature plasticity while having higher strengths than typical metal and plastic materials [12,13]. Due to the slow relaxation time of metallic glasses, only the local atoms deform violently under conventional stress-strain conditions, forming localized softening shear bands, which leads to rapid cracking and ultimately brittle fracture, greatly limiting the use of high-strength metallic glasses in structural materials [14–17]. The presence of Ni is beneficial to improve the plastic deformation ability of metallic glass. It has reported in the $Zr_{65-x}Nb_xCu_{17.5}Ni_{10}Al_{7.5}$ metallic glass system, the release of toxic Ni-ions could be effectively avoided when the alloy had excellent corrosion resistance, and would not be harm to human body [11]. Therefore, the development of new Ni-bearing Zr-based metallic glasses which expected to achieve better GFA and higher mechanical properties in along with good biocompatibility and corrosion resistance will become a hot topic of research.

To explore new BMG compositional systems, great efforts were made on changing atomic percentage, adding minor elements, or conducting elemental substitution [4]. As one significant method, elemental substitution is widely applied and a mass of elements have been tried to

* Corresponding authors.

1 Hongqi Shi and Hao Zhou contributed equally to this work.

E-mail addresses: dingyi@njtech.edu.cn (Y. Ding), liwenjuan@njtech.edu.cn (W. Liu).

enhance GFA and mechanical properties [18–22]. Recently, Fe substitution has been conducted to solve the brittleness problem and allergy aspects of BMGs [5,23–25]. On one hand, Fe has a similar weight and atomic radius with Ni, as they are all belong to VIII-group. Furthermore, Fe has a negative mixing enthalpy with the main matrix element Zr, which can ensure the high atomic packing density and atomic binding energies of metallic glasses, and therefore facilitate formation of amorphous structures and improve the GFA. It has proven that adding Fe to Zr-based metallic glasses is able to obtain higher ΔT_x , T_g and γ ascribed to the presence of deep eutectic points between Zr and Fe. Noted that the activation energy required for BMGs crystallization becomes greater, demonstrating a beneficial effect of Fe addition on GFA improvement. Gong P et al. found after Fe substituted Be in $Ti_{41}Zr_{25}Be_{34-x}Fe_x$ metallic glass system [23], $Ti_{41}Zr_{25}Be_{28}Fe_6$ metallic glass has the widest subcooled liquid phase region ($\Delta T_x=107$ K) with an amorphous critical size of up to 8 mm. A significant increase in yield strength, ultimate strength and plastic strain from 1755 MPa, 1914 MPa and 2.9% to 1964 MPa, 2268 MPa and 11.2% was achieved. In addition, Fe substitution avoids the adverse effects of toxic Ni and Bi elements. Although the effect of element substitution on the thermal stability, GFA and mechanical properties of BMG has been extensively studied, the principle has not yet been explained by the fundamental theory and therefore further work is significant [25,26]. Furthermore, the influence of Fe substitution on corrosion behavior is not revealed yet and is determinant to practical utilization of new Zr-based BMGs.

In this work, Fe substitution for Ni in $Zr_{56}Cu_{24}Al_9Ni_7Ti_4$ metallic glass alloy system was conducted to address the issues of low plasticity of Zr-based BMGs and bio-toxicity of Ni elements. A series of $Zr_{56}Cu_{24}Al_9Ni_{7-x}Ti_4Fe_x$ ($x = 0, 1, 3, 5, 7$ at.%) BMGs with a diameter of 2 mm were successfully prepared. Firstly, the effect of Fe substitution were evaluated by studying the GFA, crystallization kinetics, mechanical properties. Later, we explored the corrosion behavior of as-synthesized $Zr_{56}Cu_{24}Al_9Ni_{7-x}Ti_4Fe_x$ ($x = 0, 1, 3, 5, 7$ at.%) in a simulated body fluid solution (SBF) and revealed the vital role of Fe addition on inhibition of pitting corrosion.

2. Experimental

$Zr_{56}Cu_{24}Al_9Ni_{7-x}Ti_4Fe_x$ ($x = 0, 1, 3, 5$, and 7 at.%) ingots were prepared by arc-melting a mixture of pure Zr, Cu, Al, Ni, Ti and Fe (99.9%) under an argon atmosphere in the arc furnace. The ingots were remelted at least five times to ensure the composition is homogeneous. The melted ingots were cast into the cylindrical rod with 2 mm diameter and the length of 100 mm by the injection copper mold casting method under high-purity argon atmosphere. The structures of as-cast alloys were characterized by an X-ray diffraction (XRD, ARL X'TRA) with $CuK\alpha$ radiation at a scan rate of 2 °/min and within 20°–80°. The thermodynamic and kinetic properties were measured by differential scanning calorimetry (DSC, NETZSCH DSC204) at a heat rate of 10 K/min from room temperature to 1273 K under a flowing high-purity argon. In order to ensure the repeatability of experiments, all the ingots were cut into 15–20 mg and ultrasonically cleaned in alcohol for 15 min. For analyzing the mechanical properties of BMGs, uniaxial compression tests were performed using an electronic universal testing machine (Z010UTM) with an initial engineering strain rate of 10^{-2} mm/s at room temperature. The compressive samples were 2 mm in diameter and 4 mm in length.

The electrochemical behavior of BMGs was evaluated in a simulated body fluid (SBF) solution ($pH=7.35$) at 37.5 °C by using CHI660E electrochemical workstation. The working electrode (WE) was made by cutting a 2 mm sample in appropriate length and encapsulating it with epoxy resin in PVC hollow tube. The contact area of WE is 3.14 mm^2 . A saturated calomel electrode (SCE) and a Pt plate were respectively used as the reference electrode and counter electrode. Before the potentiodynamic polarization and the first EIS measurements (marked as 0 h), the open circuit potential (OCP) was monitored about 30 min until it

became stable. Electrochemical impedance spectrum (EIS) measurements were performed in the frequency range from 100 kHz to 10 MHz at the OCP with a potential perturbation of ±10 mV. Furthermore, potential-dynamic polarization tests were conducted at a potential sweep rate of 0.5 mV/s in a potential range from −600 mV (vs SCE) to 400 mV (vs SCE). Finally, lateral surfaces, fracture morphology, and corrosion morphology of BMGs after compressive and electrochemical tests were characterized by a scanning electron microscope (SEM, JSM-6510). Meanwhile, element composition on the surface of Zr-based alloys was analyzed with energy dispersive X-ray spectroscopy (EDS) after electrochemical corrosion.

3. Results and discussion

3.1. Structure

The XRD patterns of $Zr_{56}Cu_{24}Al_9Ni_{7-x}Ti_4Fe_x$ ($x = 0, 1, 3, 5$, and 7 at.%) alloys with 2 mm diameters after Ni replacement with Fe is depicted in Fig. 1. It is obvious that XRD patterns of BMGs with Fe contents of 0, 1 and 3 at.% show a single broad diffuse halo peak at 35–40°, indicating the formation of amorphous structure. However, various crystalline phases including Al_3Ni , $AlZr_3$, $CuZr_2$, $Cu_{10}Zr_7$ and $CuTi$ were found when Fe contents increased to 5 and 7 at.%. Sharp Bragg diffraction peaks were observed after complete substitution Ni with Fe. Therefore, the limit content of metallic glass formed by substitution of Ni with Fe should be about 3 to 5 at.%. The excess Fe leads to a disability of forming the amorphous structure under rapid cooling conditions due to the positive enthalpy of mixing between Cu and Fe ($\Delta H_{mix}=13 \text{ kJ/mol}$), and thus results in the formation of crystalline phase and its separation from the matrix.

3.2. Glass-forming ability

Fig. 2 presents the DSC curves of the as-cast $Zr_{56}Cu_{24}Al_9Ni_{7-x}Ti_4Fe_x$ ($x = 0, 1, 3, 5$, and 7 at.%) alloys at a heating rate of 10 K/min. The melting and crystallization behaviors of $Zr_{56}Cu_{24}Al_9Ni_{7-x}Ti_4Fe_x$ alloys were revealed in the DSC curves, where the onset temperature of crystallization (T_x), glass transition temperature (T_g), melting temperature (T_m), and liquid temperature (T_l) are marked by arrows. The DSC curves of the Zr-based BMGs after Fe substitution for Ni ($x = 0, 1, 3$ at.%) show a clear endothermic behavior (glass transition) and a clear exothermic behavior (crystallization). Two distinct exothermic peaks can be observed in the endothermic behavior, indicating a two-step crystallization process during the heating process and a two-step melting process

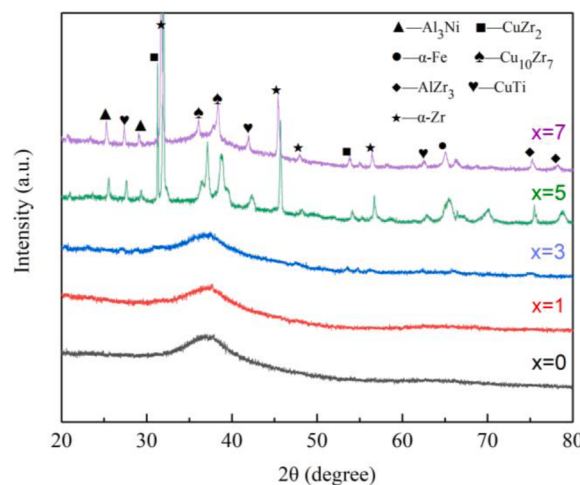


Fig. 1. XRD patterns of as-cast $Zr_{56}Cu_{24}Al_9Ni_{7-x}Ti_4Fe_x$ ($x = 0, 1, 3, 5$, and 7 at.%) alloys with diameters of 2 mm.

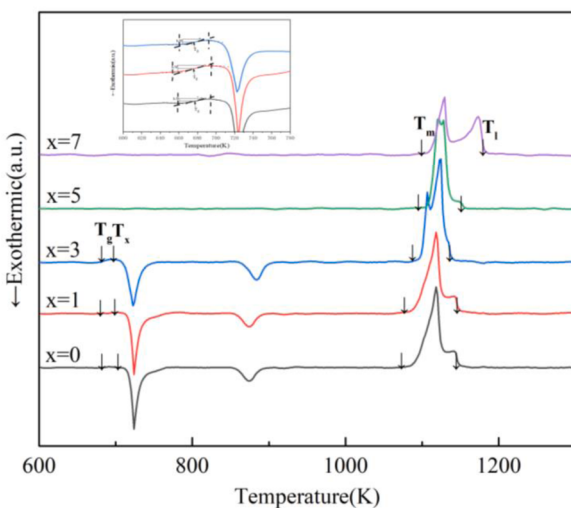


Fig. 2. DSC curves for $Zr_{56}Cu_{24}Al_9Ni_{7-x}Ti_4Fe_x$ ($x = 0, 1, 3, 5$, and 7 at.%) alloys at a heating rate of 10 K/min.

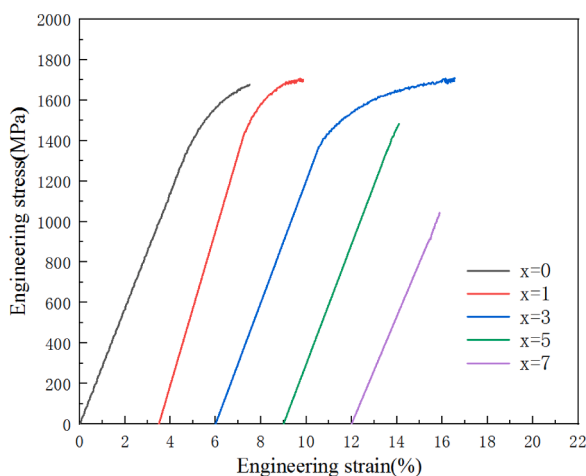


Fig. 3. Compressive stress-strain curves of the as-cast $Zr_{56}Cu_{24}Al_9Ni_{7-x}Ti_4Fe_x$ ($x = 0, 1, 3, 5$, and 7 at.%) alloys.

during the melting of the alloys [27]. As Fe content increases, T_g , T_x of the alloys changed slightly, while T_m increases and T_l decreases firstly and rises again. That is because the atomic radius of Fe element is smaller than that of Ni, the increase in Fe element makes the microstructure of alloys more chaotic and therefore requires more energy for the phase change to occur, accordingly resulting in a change of each thermal parameter.

In addition, characteristic parameters including the glass transition temperature (T_g), the onset crystallization temperature (T_x), the supercooled liquid region ($\Delta T_x = T_x - T_g$), the onset melting temperature (T_m), the liquid temperature (T_l), and other thermal stability parameters are summarized in Table 1. The thermal parameter T_{rg} ($T_{rg} = T_g/T_m$)

Table 1

Thermal stability parameters for as-cast $Zr_{56}Cu_{24}Al_9Ni_{7-x}Ti_4Fe_x$ ($x = 0, 1, 3, 5$, and 7 at.%) alloys.

Alloys	T_g/K	T_x/K	T_m/K	T_l/K	ΔT_x	T_{rg}	γ
$x = 0$	678	710	1078	1161	32	0.629	0.386
$x = 1$	680	708	1081	1158	28	0.629	0.385
$x = 3$	678	706	1089	1151	28	0.623	0.386
$x = 5$	—	—	1100	1156	—	—	—
$x = 7$	—	—	1101	1191	—	—	—

Table 2

Compressive parameters of $Zr_{56}Cu_{24}Al_9Ni_{7-x}Ti_4Fe_x$ ($x = 0, 1, 3, 5$, and 7 at.%) alloys.

Alloys	σ_{max} (MPa)	ε_e (%)	ε_p (%)	ε (%)
$x = 0$	1677	6.28	1.22	7.50
$x = 1$	1702	4.46	1.90	6.36
$x = 3$	1709	5.00	5.55	10.55
$x = 5$	1484	5.10	0	5.10
$x = 7$	1043	3.89	0	3.89

generally indicates a reduction in the glass transition temperature while γ ($= T_x/(T_g + T_l)$) provides an indication of the GFA of metallic glass. The T_{rg} and γ varied similarly with the same heating rate. It is generally that all three parameters, ΔT_x , T_{rg} and γ , reflect the GFA and the thermal stability of the supercooled liquid [7,28,29]. Normally, the larger the parameter is, the more difficult the process of nucleation and growth of the alloy melt during supercooled solidification and crystallization would be, the smaller the critical cooling rate required, and the greater the glass-forming ability would be. According to the DSC and XRD results of $Zr_{56}Cu_{24}Al_9Ni_{7-x}Ti_4Fe_x$ alloys, it is obvious that the addition of Fe to 3% causes similar GFA and thermal stability capability as indicated from ΔT_x , T_{rg} and γ values.

In general, the high GFA of metallic glass requires complex component compositions, large atomic size differences and negative heat of mixing. Firstly, the melt entropy difference of alloys and the atomic arrangement density after melting are proportional to the number of group elements, so a multi-group element composition with Fe added has a higher melt entropy. Meanwhile, larger atomic size difference will induce a higher melt entropy value, and more complex crystallization products. Simultaneously, metallic glass subcooling melt tends to be more viscous. As a result, the melt atoms are difficult to diffuse, become denser arrangement, and inhibit the nucleation growth process, therefore obtaining greater amorphous formation capacity. Then, in this new Zr-Cu-Al-Ni-Ti-Fe system, the atomic radius of Zr, Cu, Al, Ni, Ti, and Fe are 0.160 nm, 0.128 nm, 0.143 nm, 0.124 nm, 0.145 nm, and 0.124 nm in order. Obviously, atomic size ratios of Fe and Ni are essentially similar, but their heat of mixing differs significantly. Therefore, trace addition of Fe element would give rise to more chaotic internal structure of the composition system, as a result the alloy would require higher activation energy during cooling and crystallization, and be conducive to the formation of an amorphous structure. However as excess Fe added, the heats of mixing for Zr-Ni, Zr-Fe, Cu-Ni, and Cu-Fe are -49 , -25 , 4 , and 13 kJ/mol respectively, the heats of mixing for Fe relative to the main components Zr and Cu are much larger than those for Ni, which reduces the atomic packing density and affects the GFA of the alloy, making the alloy more susceptible to crystallization during subcooling. It is also evident from the clearer two-step endothermic crystallization process that the addition of elemental Fe may promote the formation of an icosahedral short-range ordered structure, which is conducive to thermal stability.

3.3. Mechanical properties

After uniaxial compression experiments, the compressive stress-strain curves of $Zr_{56}Cu_{24}Al_9Ni_{7-x}Ti_4Fe_x$ alloys with different Fe addition are presented in Fig. 3. Meanwhile, as the most important indicators of mechanical properties, compressive yield strength σ_y , the ultimate fracture strength σ_{max} and compressive strain ε consisting of plastic strain ε_p and elastic strain ε_e are summarized in Table 2. In the compression process, the Zr-based BMGs with Fe addition of 0, 1 at% first undergo a large elastic deformation, the stress and strain in the curve basically show a positive relationship. Subsequently, when the stress reaches a certain value (σ_y), the slope of the curve changes sharply towards 0 until fracture, indicating an obvious yielding behavior emerges and fracture occurs after various degrees of plastic deformation.

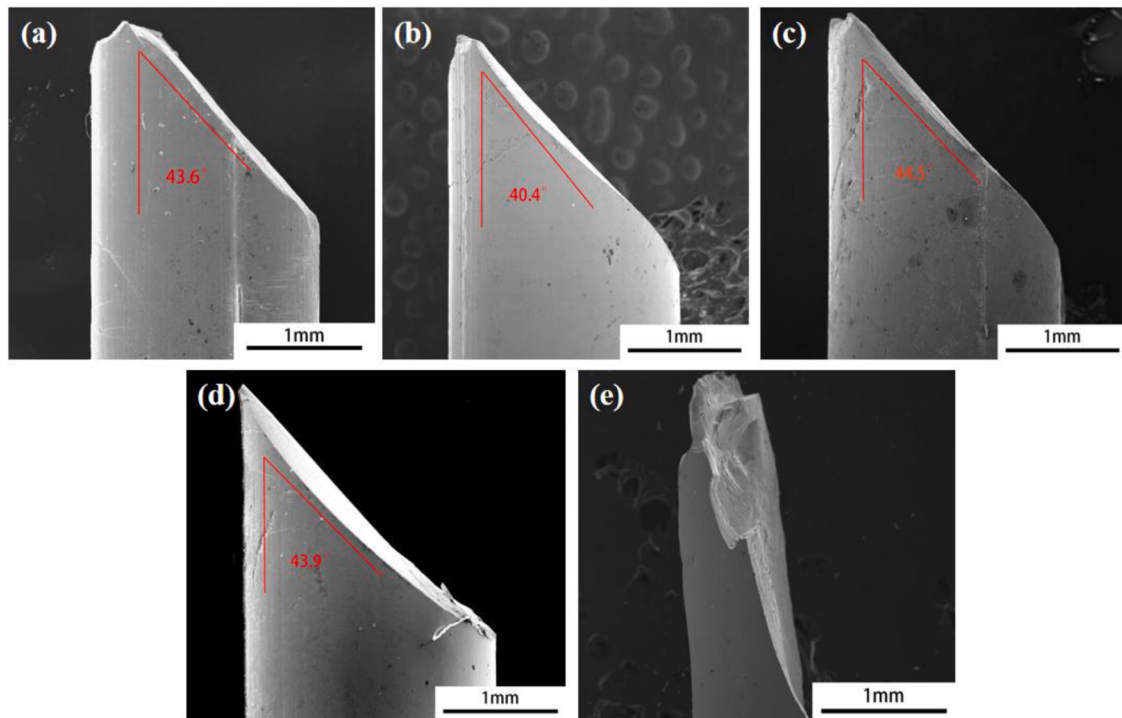


Fig. 4. Typical lateral surfaces of as-cast $Zr_{56}Cu_{24}Al_9Ni_{7-x}Ti_4Fe_x$ ($x = 0, 1, 3, 5$, and 7 at.%) alloys with the diameter of 2 mm after compression tests: (a) $x = 0$; (b) $x = 1$; (c) $x = 3$; (d) $x = 5$; (e) $x = 7$.

Table 3

Electrochemical parameters of as-cast $Zr_{56}Cu_{24}Al_9Ni_{7-x}Ti_4Fe_x$ ($x = 0, 1, 3, 5$, and 7 at.%) alloys derived from potentiodynamic polarization curves.

Alloys	E_{corr}/V	E_{pit}/V	$ E_{corr}-E_{pit} /V$	$I_{pass}/A\cdot cm^{-2}$
$x = 0$	-0.305	0.058	0.361	7.059×10^{-8}
$x = 1$	-0.276	0.122	0.398	6.929×10^{-8}
$x = 3$	-0.333	0.213	0.546	7.120×10^{-8}
$x = 5$	-0.266	0.057	0.323	6.667×10^{-8}
$x = 7$	-0.230	-0.072	0.302	6.936×10^{-7}

Notably, the pristine alloy $Zr_{56}Cu_{24}Al_9Ni_7Ti_4$ has a low σ_{max} of 1677 MPa and a poor plastic strain ϵ_p of 1.22% . With Fe content increasing to 3 at.%, both compressive strength and plasticity are significantly enhanced and reach their maximum values (σ_{max} and ϵ_p are 1709 MPa and 5.55% , respectively). However, at 5 and 7 at.% Fe substitution, the alloys only show brittle fracture behavior and fracture occurred directly without any plastic deformation. It is therefore concluded in $Zr_{56}Cu_{24}Al_9Ni_{7-x}Ti_4Fe_x$ system, 3 at.% Fe replacing Ni brings the optimum compressive strength and plasticity performance compared to the pristine alloy. This indicates the substitution of Ni with an appropriate amount of Fe can effectively increase the plastic deformation capacity of the alloy at room temperature without reducing its original strength.

Generally, adding new elements, which have a positive heat of mixing with atoms in the amorphous alloy system, can improve the plasticity of the alloy. It is found adding positive mixing heat elements cause local chemistry and free volume inhomogeneities [30]. These inhomogeneities could serve as both the starting point and the obstacle point for the proliferation of the shear band. These two opposite effects lead to the nucleation and proliferation of the shear band, resulting in greater plasticity of the alloy [31]. Therefore, Fe addition could increase plastic strain of amorphous alloys, which attributed to the mutual repulsion between Fe and Cu atoms, and a positive mixing heat of 13 KJ/mol between the two atoms [32].

Moreover, the fracture flanks of the metallic glasses at room temperature were further characterized to better evaluate the deformation

mechanisms Fig. 4. According to the Mohr-Coulomb standard [33], in uniaxial compression experiments, the fracture angle generally deviates from the plane of maximum shear stress, i.e. the 45° angle plane. Thus, the resulting inclined fracture angles were 43.6% , 40.4% , 44.5% and 43.9% for metallic glass with a Fe content of 0 , 1 , 3 , 5 at.%, respectively. But the Zr-based alloy with 7 at.% Fe exhibits a split cross section from the middle of the compression test due to the poor flow filling ability of alloys under fast cooling solidification conditions, resulting in a mass of internal casting defects. The fracture angle is biased in the axial direction and the fracture angle is less than 45° , because at the instant of uniaxial pressure fracture of the alloy the shear normal stress is opposite to the shear fracture instant normal stress.

In addition, the fracture morphologies of five as-cast $Zr_{56}Cu_{24}Al_9Ni_{7-x}Ti_4Fe_x$ alloys after the compression test were presented. Fig. 5 shows two different morphologies, the typical vein pattern and the gully pattern: shear fracture and crushing fracture of metallic glass. The two types of fracture are related to the shear strength and fracture strength of alloys. As the mechanical properties decrease, shear fracture will gradually change to crushing fracture and plasticity will decrease. A large number of well-developed vein-like morphology extending along the shear stress direction were observed in Fig. 5b&c. Plenty of regular and higher density vein-like patterns were observed when Fe substitution content reaches 3 at.%, followed by 1 at.% Fe addition, confirming a pure shear fracture process for Zr-based BMGs with low amount of Fe. Moreover, $Zr_{56}Cu_{24}Al_9Ni_4Ti_4Fe_3$ alloy shows a smaller and more densely distributed tough nest size and a large number of secondary shear zones splitting around the primary shear zone, which is consistent with its superior compressive plasticity.

According to the free volume model [34,35], atoms move into the adjacent voids and form new vacancies under the action of stress concentration and elastic strain [36], therefore inducing to a specific morphology. The increase in vacancies, which is free volume, causes the meta-stable metallic glasses to melt and form a viscous flow at the moment of fracture when the stress is applied, creating a vein-like pattern of the fracture [37]. The more free volume there is, the more shear zones are formed, which effectively prevents the formation and

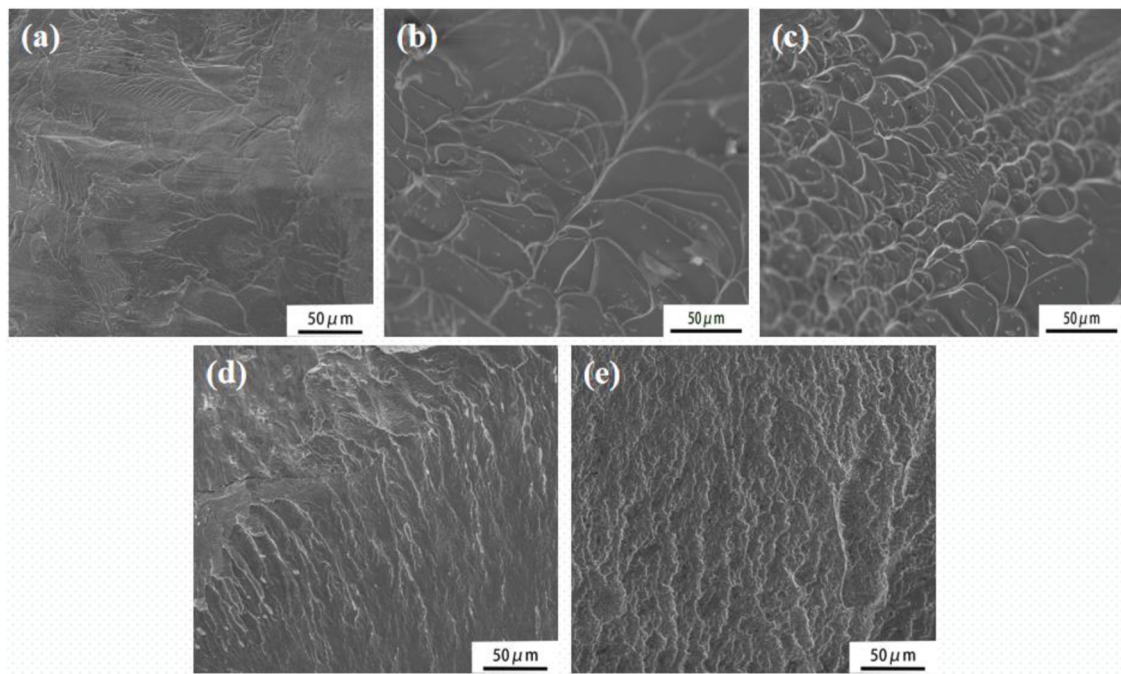


Fig. 5. SEM images of the fracture morphology for as-cast $Zr_{56}Cu_{24}Al_9Ni_{7-x}Ti_4Fe_x$ ($x = 0, 1, 3, 5$, and 7 at.%) alloys under compressive deformation: (a) $x = 0$; (b) $x = 1$; (c) $x = 3$; (d) $x = 5$; (e) $x = 7$.

expansion of cracks and allows plasticity to be enhanced. The Zr-based BMGs with 1 and 3 at.% Fe addition also show numerous smooth areas typical of shear offset. However, at 0, 5, and 7 at.% Fe, the fracture behavior appears as brittle fracture. The fracture profile exhibits an uneven surface with river-like and gully-like patterns which attributed to smaller positive compressive breaking strength than the shear strength during fracture [38], as the positive stress is greater than the shear stress. Therefore the shear deformation is more difficult and worse plasticity under the effect of amorphous internal structural inhomogeneity.

Overall, the fracture strength and compressive plasticity of the as-cast $Zr_{56}Cu_{24}Al_9Ni_{7-x}Ti_4Fe_x$ ($x = 0, 1, 3, 5$, and 7 at.%) alloys are significantly affected by Fe substitution and demonstrate a first increase and then decrease trend with raising Fe amount. The optimum mechanical properties are found in $Zr_{56}Cu_{24}Al_9Ni_4Ti_4Fe_3$ alloy, with a compressive strength and plasticity of 1709 MPa and 5.548% respectively, and a large number of small, dense, vein-like tough nests are shown in the fracture pattern because of the enhanced plasticity.

3.4. Electrochemical behaviors

To evaluate the effect of Fe substitution on the corrosion behavior of $Zr_{56}Cu_{24}Al_9Ni_{7-x}Ti_4Fe_x$ ($x = 0, 1, 3, 5$, and 7 at.%) alloys, the potentiodynamic polarization measurements were conducted in SBF solution at 35.7 °C and the results are given in Fig. 6. Traditional Ti6Al4V alloy was used as a control sample. As can be seen from the polarization curves, $Zr_{56}Cu_{24}Al_9Ni_{7-x}Ti_4Fe_x$ ($x = 0, 1, 3, 5$, and 7 at.%) alloys show similar electrochemical behaviors. All the Zr-based alloys enter a wide passive region after spontaneously passivated and then suffer from a pitting corrosion with the increase in applied potential because of the breaking of passive film caused by the presence of active Cl^- in SBF solution. However, there is no passivation behavior for Ti6Al4V alloy in along with a much higher corrosion current density, indicating its inferior corrosion performance in comparison with Zr-based alloys. Electrochemical parameters of as-cast $Zr_{56}Cu_{24}Al_9Ni_{7-x}Ti_4Fe_x$ alloys derived from potentiodynamic polarization curves are shown in Table 3. Because of the presence of passivation behaviors for Zr-based alloy, the

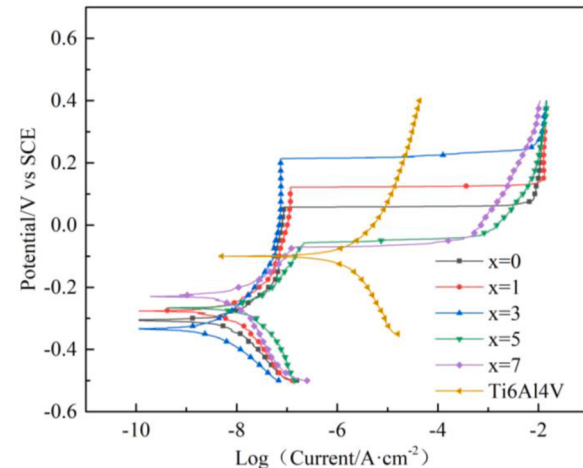


Fig. 6. Polarization curves for $Zr_{56}Cu_{24}Al_9Ni_{7-x}Ti_4Fe_x$ ($x = 0, 1, 3, 5$, and 7 at.%) and Ti6Al4V alloys in SBF solution at 35.7 °C.

kinetics of dimensional passive current density (I_{pass}), the corrosion potential (E_{corr}), the pitting potential (E_{pit}), and the passivation zone ($|E_{corr}-E_{pit}|$) were obtained to evaluate their passivation ability. It is noticed that the dimensional passive current densities of the Zr-based BMGs with different Fe addition are all in a lower order of magnitude ($10^{-7}\sim 10^{-8} A/cm^2$), illustrating a good corrosion resistance in SBF solution. It is noticed that all the Fe substituted Zr-based BMGs exhibits similar potentials with pristine Zr BMG, demonstrating a similar corrosion tendency in thermodynamics. However, difference in Fe content leads to variation in E_{pit} and $|E_{corr}-E_{pit}|$, both of which are the key parameters for pitting corrosion. In general, it is believed that a higher E_{pit} indicates a lower pitting probability of passive film and that a wider passivation zone of $|E_{corr}-E_{pit}|$ represents a better passivation stability. At 3 at.% Fe replacing Ni, the pitting potential is 0.213 V and the passivation zone width is 546 mV, indicating $Zr_{56}Cu_{24}Al_9Ni_4Ti_4Fe_3$ alloy is the most resistant to pitting corrosion in a SBF solution environment.

As reported, the more corrosion resistant the metallic glass is, the denser and more stable the passive film formed in the solution and the less likely to form pitting defects [39]. Accordingly, with trace addition of Fe, the passive oxide film of Fe compensates for some defects in the Zr passive film, correspondingly enhancing the corrosion resistance of BMGs. But with more Fe addition, the E_{pit} shifts to negative values and the passivation zone becomes narrowed ascribed to a defective and non-dense passive film generated during more Fe addition, reducing the strength of the passive film and leading to a reduction in corrosion resistance [40].

The EIS, as a non-destructive method, shows the evolution of the corrosion behavior of BMGs occurring for a short time in SBF solution after Fe substitution for Ni. The Nyquist and Bode plots for $\text{Zr}_{56}\text{Cu}_{24}\text{Al}_9\text{Ni}_{7-x}\text{Ti}_4\text{Fe}_x$ ($x = 0, 1, 3, 5$, and 7 at.%) alloys are shown in Fig. 7. From the Nyquist plot, it can be seen only a single capacitive semicircular arc is evolved, revealing a stable formation of passive surface film during the immersion. Furthermore, Bode plots also confirm the corrosion behavior is controlled by a time constant with phase angles' values approached to 90° , indicating the generation of smooth surface film [41]. A simple equivalent electrical circuit composed of $[R_s(QR_{ct})]$ shown is utilized to fit the EIS spectra, Where R_s represents solution resistance, Q is constant phase element and R_{ct} is charge-transfer resistance. Normally, R_{ct} is the indicator of corrosion resistance, the larger the R_{ct} is, the better the corrosion resistance will be. Table 4 summarizes the corresponding corrosion resistances for alloys with different Fe substitution Ni. It is obvious that the corrosion resistance is improved by increasing Fe content and 3 at.% Fe addition leads to the best corrosion resistance. But R_{ct} decrease greatly by further increasing Fe addition to 5 and 7 at.%, suggesting a detrimental effect of excess Fe. EIS results are basically consistent with potentiodynamic polarization measurement, indicating that a suitable amount of Fe

replaces Ni elements could enhance the corrosion resistance of Zr-based BMGs due to the formation of compact passive film.

In addition, the typical corrosion morphologies of Zr-based alloys after polarization experiments are characterized by SEM and shown in the Fig. 8. It is known Zr-based BMGs would suffer pitting corrosion in Cl^- containing environments. Generally, Al, Ti and Zr in the $\text{Zr}_{56}\text{Cu}_{24}\text{Al}_9\text{Ni}_{7-x}\text{Ti}_4\text{Fe}_x$ alloy system has a tendency to form passive films during the anodic polarization process. Actually, a stable and dense of Zr oxide is mainly formed due to the dominated Zr composition, promoting the formation of passive film. However, Cl^- in the SBF solution would pass through the defects in the passive film, causing the film to erupt and damage step by step, eventually forming pitting corrosion and expanding into the corrosion pits. As indicated in Fig. 8(b) and (e), obvious pitting defects are observed when added 1 and 7 at.% Fe, demonstrating the broken passive films resulted from insufficient dosage and excess addition of Fe. However, the surface of Zr-based alloy in Fig. 8(c) is essentially free of pitting, with only a few pits appearing in the peripheral part, while the pristine alloy and alloy with 5 at.% Fe addition have a variety of smaller pits on the surface, indicating a somewhat protection of passive film. Noticeably, the pitting corrosion becomes the severest when substituting Ni with 7 at.% Fe, with visible corrosion products over the pitting defects, confirming the total replacement of Ni with Fe destructed the compactness of the passive film and leading to the worst corrosion resistance, basically in agreement with electrochemical measurement results.

Furthermore, the element compositions of as-cast Zr-based alloys over the pits and free of pits were analyzed after polarization tests and the results are shown in Table 5. It is clear that after the anodic polarization process, all the Zr-based alloys were oxidized with higher content of Zr oxides. Meanwhile, the amount of Cu is increased from 10.0% to 64.9 wt%, indicating a poor corrosion resistance after excess Fe

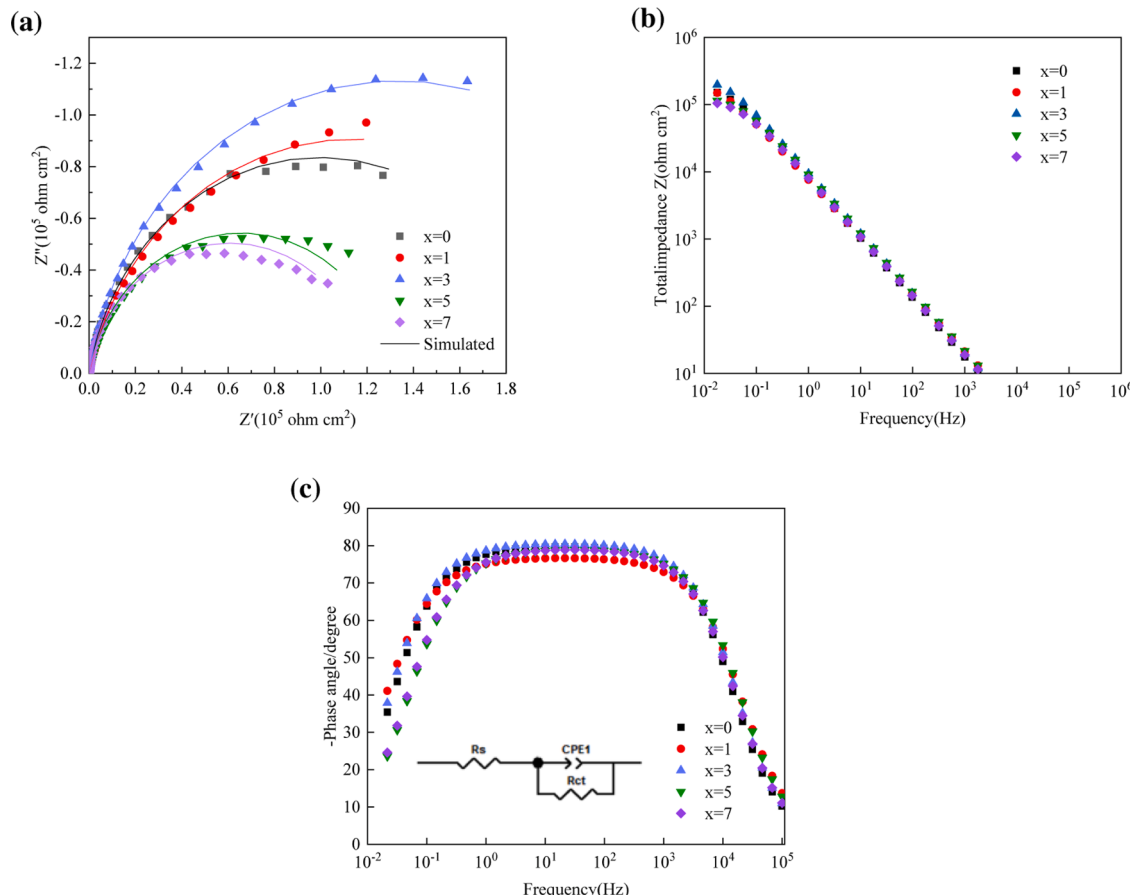


Fig. 7. Nyquist and Bode plots of $\text{Zr}_{56}\text{Cu}_{24}\text{Al}_9\text{Ni}_{7-x}\text{Ti}_4\text{Fe}_x$ ($x = 0, 1, 3, 5$, and 7 at.%) alloys in SBF solution at 35.7 $^\circ\text{C}$.

Table 4

Simulated parameters of the as-cast $Zr_{56}Cu_{24}Al_9Ni_{7-x}Ti_4Fe_x$ ($x = 0, 1, 3, 5$, and 7 at.%) alloys derived from EIS curves.

Alloys	$R_s/\Omega\bullet cm^{-2}$	Error/%	$Q/S\bullet Sec^n$	Error/%	n	Error/%	$R_{ct}/\Omega\bullet cm^{-2}$	Error/%
$x = 0$	1.52	3.65	2.45×10^{-5}	3.48	0.90	0.61	1.99×10^5	4.66
$x = 1$	1.53	3.81	2.72×10^{-5}	2.63	0.85	0.47	2.28×10^5	5.04
$x = 3$	1.54	3.53	2.03×10^{-5}	3.54	0.90	0.61	2.67×10^5	4.67
$x = 5$	1.52	3.75	2.14×10^{-5}	2.81	0.88	0.48	1.31×10^5	3.36
$x = 7$	1.55	3.91	2.43×10^{-5}	4.76	0.88	0.82	1.22×10^5	4.25

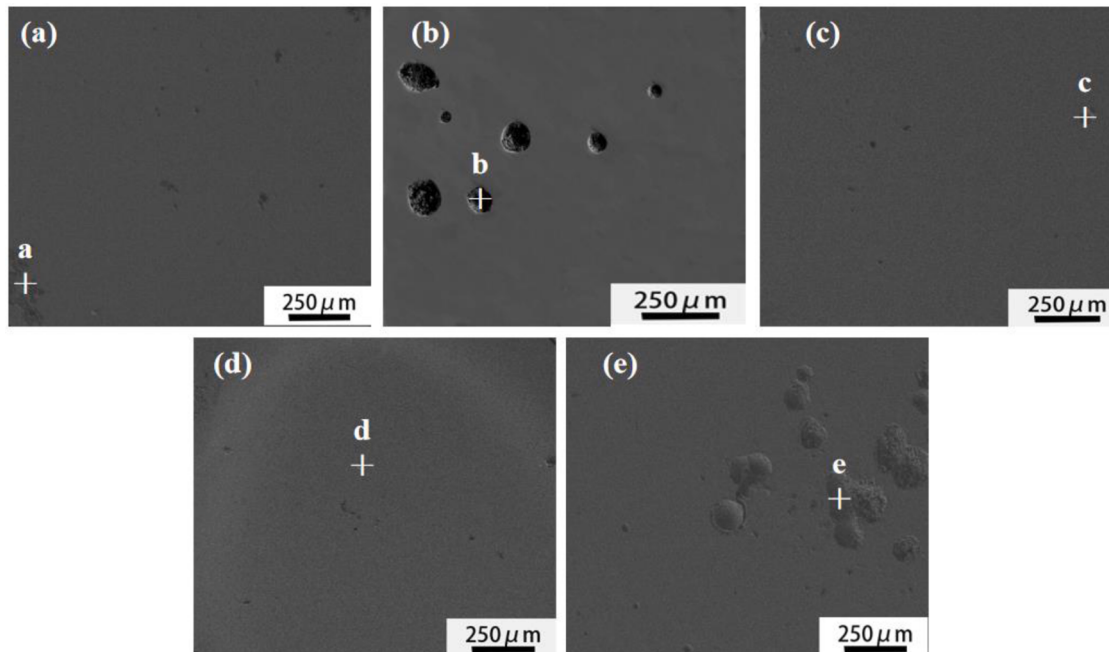


Fig. 8. SEM images of corrosion morphology for as-cast $Zr_{56}Cu_{24}Al_9Ni_{7-x}Ti_4Fe_x$ ($x = 0, 1, 3, 5$, and 7 at.%) alloys under compressive deformation: (a) $x = 0$; (b) $x = 1$; (c) $x = 3$; (d) $x = 5$; (e) $x = 7$.

Table 5

Element compositions on $Zr_{56}Cu_{24}Al_9Ni_{7-x}Ti_4Fe_x$ ($x = 0, 1, 3, 5$, and 7 at.%) alloys after polarization test: (a) $x = 0$; (b) $x = 1$; (c) $x = 3$; (d) $x = 5$; (e) $x = 7$.

Element (wt.%)	Zr	Cu	Al	Ni	Fe	Ti	Cl	O
a	20.6	10.0	4.4	3.6	—	—	1.7	57.5
b	28.3	24.4	4.1	4.8	4.2	1.8	—	32.4
c	16.6	23.2	5.1	1.6	0.9	1.3	2.2	49.4
d	20.5	20.2	3.6	1.2	1.0	1.8	4.0	47.5
e	10.9	64.9	3.9	—	4.1	1.9	1.0	25.2

addition. The higher standard electrode potential of Cu compared to Zr and other elements results in the formation of galvanic couples, thus accelerating the corrosion rate. Nevertheless, a large amount of Fe with 4.1 wt.% in addition to Cu of 64.9 wt.% is existed in $Zr_{56}Cu_{24}Al_9Ti_4Fe_7$. Correspondingly, the presence of less Fe in the Zr-based alloys indicates a more protection and the relative higher corrosion performance. It is indicated the spots of "a and d" in pristine alloy and $Zr_{56}Cu_{24}Al_9Ni_2-Ti_4Fe_5$ alloy has a relatively lower content of Fe, proving a good resistance to pitting corrosion. Specifically, the surface film at spot "c" is only composed of 0.9 wt.% Fe, further facilitates oxide film and enhances the pitting corrosion resistance. Therefore, replacement of Ni by Fe at around 3 at.% is to a certain extent conducive to enhance resistance to pitting.

Overall, suitable Fe substitution enhanced the corrosion resistance of Zr-based alloys. On one hand, trace addition of Fe improve the internal structure disorder of the alloy, and the more disordered structure can hinder the corrosion process to a certain extent [42]. Furthermore, when

ZrO_2 -rich passivation film is generated on the alloy surface, trace elements such as Fe, Al and Ti are beneficial to fill the defects in the passivation film to a certain extent, and hinder the penetration of Cl^- [43]. However, the addition of excessive Fe element affects the generation of dens ZrO_2 -rich passivation film, so there is no obvious passivation interval [7]. It is confirmed $Zr_{56}Cu_{24}Al_9Ni_4Ti_4Fe_3$ alloy has the optimal mechanical properties and corrosion resistance, indicating synergistic effect of Fe substitution on mechanical and corrosion performance.

4. Conclusion

In summary, a series of $Zr_{56}Cu_{24}Al_9Ni_{7-x}Ti_4Fe_x$ ($x = 0, 1, 3, 5$, and 7 at.%) BMGs were synthesized to explore the effect of Fe substitution for Ni on GFA, mechanical properties, and corrosion resistance. It is found 3 at.% Fe addition results in a change in the thermodynamic parameters and slightly affects GFA of the alloys, but excessive Fe addition to 5 and 7 at.% leads to the failure of amorphous structure and generation of diverse crystalline phases. The prepared $Zr_{56}Cu_{24}Al_9Ni_4Ti_4Fe_3$ BMG exhibits the compressive failure strength of 1709 MPa with the best compressive plastic deformation of 5.55%, higher than 1677 MPa and 1.22% of pristine $Zr_{56}Cu_{24}Al_9Ni_7Ti_4$ alloy. However, at 5 and 7 at.% Fe substitution, the Zr-based alloys only show brittle fracture behavior and fracture occurred directly without any plastic deformation. In the meantime, the electrochemical measurements demonstrate Fe substitution has a consistent effect on the corrosion resistance of the $Zr_{56}Cu_{24}Al_9Ni_{7-x}Ti_4Fe_x$ amorphous alloy in SBF solution. The $Zr_{56}Cu_{24}Al_9Ni_4Ti_4Fe_3$ BMG has the widest passive region of 564 mV, and

the pitting potential has shifted to more positive value from the original 0.058 V to 0.213 V, indicating an improved corrosion resistance of Zr-based BMGs. Moreover, the corrosion morphology indicate trace addition of Fe to $Zr_{56}Cu_{24}Al_9Ni_{7-x}Ti_4Fe_x$ BMGs greatly promotes the intactness of passive film and accordingly enhances the resistance of surface film to chloride ions attack. But over-addition of Fe results in an enrichment of Cu and Fe oxide and deteriorates the compactness of passive film, causing a poor pitting corrosion resistance. Overall, the substitution of Fe for Ni gives a synergistic effect on the mechanical and corrosion performance. The appropriate addition of Fe could improved both the GFA, mechanical properties, and corrosion resistance, while excessive additions have worsen the alloy properties.

CRediT authorship contribution statement

Hongqi Shi: Conceptualization, Methodology, Investigation. **Hao Zhou:** Data curation, Writing – original draft. **Zhenghao Zhou:** Resources. **Yi Ding:** Supervision. **Wenjuan Liu:** Supervision, Writing – review & editing. **Jin Ji:** Writing – original draft.

Declaration of Competing Interest

The authors declare that they have no known competing financial interests or personal relationships that could have appeared to influence the work reported in this paper.

Acknowledgment

This work was supported by the open fund project of innovation, entrepreneurship and practice of Nanjing Tech University (No. 201921003417). All authors declare no conflict of interest. Hongqi Shi and Hao Zhou contributed equally to this work.

Reference

- [1] W.H. Wang, C. Dong, C.H. Shek, Bulk metallic glasses, *Mat. Sci. Eng. R.* 44 (2004) 45–89.
- [2] A. Takeuchi, A. Inoue, Classification of bulk metallic glasses by atomic size difference, heat of mixing and period of constituent elements and its application to characterization of the main alloying element, *Mater. Trans.* 46 (2005) 2817–2829.
- [3] D.C. Hofmann, J. Suh, A. Wiest, G. Duan, M. Lind, M.D. Demetriou, W.L. Johnson, Designing metallic glass matrix composites with high toughness and tensile ductility, *Nature* 451 (2008) 1085–1089.
- [4] M.M. Khan, A. Nemati, Z.U. Rahman, U.H. Shah, H. Asgar, W. Haider, Recent advancements in bulk metallic glasses and their applications: a review, *Crit. Rev. Solid State* 43 (2018) 233–268.
- [5] J.J. Krizic, Bulk metallic glasses as structural materials: a review, *Adv. Eng. Mater.* 18 (2016) 1308–1331.
- [6] J.C. Qiao, Q. Wang, J.M. Pelletier, H. Kato, R. Casalini, D. Crespo, E. Pineda, Y. Yao, Y. Yang, Structural heterogeneities and mechanical behavior of amorphous alloys, *Prog. Mater. Sci.* 104 (2019) 250–329.
- [7] Y. Luo, Y. Jiang, P. Zhang, X. Wang, H. Ke, P. Zhang, A novel Ni-free Zr-based bulk metallic glass with high glass forming ability, corrosion resistance and thermal stability, *Chin. J. Mech. Eng.* 33 (2020) 1–7.
- [8] N. Espallargas, R.E. Aune, C. Torres, N. Papageorgiou, A.I. Munoz, Bulk metallic glasses (BMG) for biomedical applications—a tribocorrosion investigation of $Zr_{55}Cu_{30}Ni_5Al_{10}$ in simulated body fluid, *Wear* 301 (2013) 271–279.
- [9] A. Monfared, H. Vali, S. Faghhihi, Biocorrosion and biocompatibility of Zr-Cu-Fe-Al bulk metallic glasses, *Surf. Interface Anal.* 45 (2013) 1714–1720.
- [10] B. Li, W.C. Sun, H.N. Qi, J.W. Lv, F.L. Wang, M.Z. Ma, X.Y. Zhang, Effects of Ag substitution for Fe on glass-forming ability, crystallization kinetics, and mechanical properties of Ni-free Zr–Cu–Al–Fe bulk metallic glasses, *J. Alloys Compd.* 827 (2020), 154385.
- [11] L. Liu, C.L. Qiu, M. Sun, Q. Chen, K.C. Chan, G. Pang, Improvements in the plasticity and biocompatibility of Zr-Cu-Ni-Al bulk metallic glass by the microalloying of Nb, *Mat. Sci. Eng. A.* 448 (2007) 193–197.
- [12] A.L. Greer, Y.Q. Cheng, E. Ma, Shear bands in metallic glasses, *Mat. Sci. Eng. R.* 74 (2013) 71–132.
- [13] B.A. Sun, W.H. Wang, The fracture of bulk metallic glasses, *Prog. Mater. Sci.* 74 (2015) 211–307.
- [14] H. Shi, W. Zhao, X. Wei, Y. Ding, X. Shen, W. Liu, Effect of Ti addition on mechanical properties and corrosion resistance of Ni-free Zr-based bulk metallic glasses for potential biomedical applications, *J. Alloys Compd.* 815 (2020), 152636.
- [15] H. Shi, Z. Li, Z. Hu, Y. Ding, T. Tang, X. Shen, Enhancing strength and plasticity of Zr-based bulk metallic glasses by Zr partially substituted Fe and isothermal annealing, *J. Non-Cryst. Solids* 543 (2020), 120163.
- [16] R. Maass, J.F. Loeffler, Shear-band dynamics in metallic glasses, *Adv. Funct. Mater.* 25 (2015) 2353–2368.
- [17] H.L. Peng, M.Z. Li, W.H. Wang, Structural signature of plastic deformation in metallic glasses, *Phys. Rev. Lett.* 106 (2011), 135503.
- [18] A.H. Cai, Y. Feng, D.W. Ding, Y. Liu, H. Wu, Q. An, H. Ning, G.J. Zhou, Y.Y. Peng, Effect of Fe-C alloy additions on properties of Cu-Zr-Ti metallic glasses, *J. Alloy. Compd.* 798 (2019) 273–279.
- [19] Z.S. Jin, Y.J. Yang, Z.P. Zhang, X.Z. Ma, J.W. Lv, F.L. Wang, M.Z. Ma, X.Y. Zhang, R.P. Liu, Effect of Hf substitution Cu on glass-forming ability, mechanical properties and corrosion resistance of Ni-free Zr-Ti-Cu-Al bulk metallic glasses, *J. Alloy. Compd.* 806 (2019) 668–675.
- [20] H. Shi, Y. Ding, X. Shen, Incorporation of ultrafine nanograins in Zr-Cu-Al-Ni-Co bulk metallic glass enabling significantly improved mechanical properties, *Mater. Res. Express.* 6 (2019), 085211.
- [21] P. Gebara, Z. Sniadecki, Structure, magnetocaloric properties and thermodynamic modeling of enthalpies of formation of (Mn, X)-Co-Ge (X=Zr, Pd) alloys, *J. Alloy. Compd.* 796 (2019) 153–159.
- [22] S. Liu, S. Sun, K. Li, H. Li, X. Huang, G. Tu, The effect of Y addition on the crystallization behaviors of Zr-Cu-Ni-Al bulk metallic glasses, *J. Alloy. Compd.* 799 (2019) 501–512.
- [23] G. Liu, S. Kou, C. Li, Y. Zhao, H. Suo, Effect of minor Fe addition on glass forming ability and mechanical properties of $Zr_{55}Al_{10}Ni_5Cu_{30}$ bulk metallic glass, *T. Nonferr. Metal. Soc.* 22 (2012) 590–595.
- [24] P. Gong, K.F. Yao, Y. Shao, Effects of Fe addition on glass-forming ability and mechanical properties of Ti-Zr-Be bulk metallic glass, *J. Alloy. Compd.* 536 (2012) 26–29.
- [25] D.Q. Zhao, Y. Zhang, M.X. Pan, W.H. Wang, The effects of iron addition on the glass-forming ability and properties of Zr-Ti-Cu-Ni-Be-Fe bulk metallic glass, *Mater. Trans., JIM* 41 (2000) 1427–1431.
- [26] G. Choudhuri, M.K. Kumar, K. Jagannath, V. Kain, D. Srivastava, S. Basu, B.K. Shah, N. Saibaba, G.K. Dey, Influence of Fe content on corrosion and hydrogen pick up behavior of $Zr_{2.5}Nb$ pressure tube material, *J. Nucl. Mater.* 441 (2013) 178–189.
- [27] Y.J. Yang, B.Y. Cheng, Z.S. Jin, H.X. Gao, M.Z. Ma, X.Y. Zhang, Crystallization kinetics and mechanical properties of $Zr_{56}Cu_{24}Al_9Ni_{7-x}Ti_4Ag_x$ ($x=0, 1, 3, 5$, and 7) metallic glasses, *J. Alloys Compd.* 816 (2020), 152589.
- [28] M.S. Jo, J.K. Lee, Crystallization behavior of $Zr_{62}Al_8Ni_{13}Cu_{17}$ metallic glass, *Arch. Metall. Mater.* 62 (2017) 1023–1026.
- [29] J.C. Qiao, J.M. Pelletier, Isochronal and isothermal crystallization in $Zr_{55}Cu_{30}Ni_5Al_{10}$ bulk metallic glass, *T. Nonferr. Metal. Soc.* 22 (2012) 577–584.
- [30] E.S. Park, J.S. Kyewong, D.H. Kim, Enhanced glass forming ability and plasticity in Mg-based bulk metallic glasses, *Mat. Sci. Eng. A.* 449 (2007) 225–229.
- [31] Z. Liu, K.C. Chan, L. Liu, Enhanced glass forming ability and plasticity of a Ni-free Zr-based bulk metallic glass, *J. Alloys Compd.* 487 (2009) 152–156.
- [32] Q.S. Zhang, W. Zhang, A. Inoue, Ni-free Zr-Fe-Al-Cu bulk metallic glasses with high glass-forming ability, *Scripta Mater.* 61 (3) (2009) 241–244.
- [33] J. Caris, J.J. Lewandowski, Pressure effects on metallic glasses, *Acta Mater.* 58 (2010) 1026–1036.
- [34] J.X. Zhao, Y.W. Yun, Y. Jiang, J. Gong, A macro-and microscopic model characterizing unstable shear banding in metallic glass, *Mater. Res. Express.* 6 (2019), 106580.
- [35] N. Li, L. Liu, Q. Chen, J. Pan, K.C. Chan, The effect of free volume on the deformation behaviour of a Zr-based metallic glass under nanoindentation, *J. Phys. D Appl. Phys.* 40 (2007) 6055–6059.
- [36] H. Shao, Y. Xu, B. Shi, C. Yu, H. Hahn, H. Gleiter, J. Li, High density of shear bands and enhanced free volume induced in $Zr_{70}Cu_{20}Ni_{10}$ metallic glass by high-energy ball milling, *J. Alloy. Compd.* 548 (2013) 77–81.
- [37] M.M. Trexler, N.N. Thadhani, Mechanical properties of bulk metallic glasses, *Prog. Mater. Sci.* 55 (2010) 759–839.
- [38] X.K. Xi, D.Q. Zhao, M.X. Pan, W.H. Wang, Y. Wu, J.J. Lewandowski, Fracture of brittle metallic glasses: brittleness or plasticity, *Phys. Rev. Lett.* 94 (2005), 125510.
- [39] D. Zander, U. Koster, Corrosion of amorphous and nanocrystalline Zr-based alloys, *Mat. Sci. Eng. A-Struct.* 375 (2004) 53–59.
- [40] U.K. Mudali, S. Baunack, J. Eckert, L. Schultz, A. Gebert, Pitting corrosion of bulk glass-forming zirconium-based alloys, *J. Alloy. Compd.* 377 (2004) 290–297.
- [41] J. Luo, H.P. Duan, C.L. Ma, S.J. Pang, T. Zhang, Effects of yttrium and erbium additions on glass-forming ability and mechanical properties of bulk glassy Zr-Al-Ni-Cu alloys, *Mater. Trans.* 47 (2006) 450–453.
- [42] A. Monfared, S. Faghhihi, H. Karami, Biocorrosion and surface wettability of Ni-free Zr-based bulk metallic glasses, *Int. J. Electrochem. Sci.* 8 (2013) 7744–7752.
- [43] S.F. Guo, H.J. Zhang, Z. Liu, W. Chen, S.F. Xie, Corrosion resistances of amorphous and crystalline Zr-based alloys in simulated seawater, *Electrochim. Commun.* 24 (2012) 39–42.